Near-infrared metal-semiconductor-metal photodetector based on semi-insulating GaAs and interdigital electrodes

A. I. Nusir,[1,*] A. M. Hill,[2] M. O. Manasreh,[1] and J. B. Herzog[2]

[1]*Electrical Engineering Department, University of Arkansas, Fayetteville, Arkansas 72701, USA*
[2]*Department of Physics, University of Arkansas, Fayetteville, Arkansas 72701, USA*
**Corresponding author: ainusir@email.uark.edu*

Received November 19, 2014; revised November 24, 2014; accepted November 25, 2014; posted December 1, 2014 (Doc. ID 224963); published December 12, 2014

Metal-semiconductor-metal photodetectors on semi-insulating GaAs with interdigital electrodes showed significant enhancement in the spectral response in the near-infrared region as the electrode spacing is reduced. The photocurrent for the device with 5 μm interdigital spacing is five orders of magnitude higher than the dark current, and the room temperature detectivity is on the order of 2.4×10^{12} cmHz$^{1/2}$ W^{-1} at 5 V bias. Furthermore, the spectral response of this device possesses strong dependence on the polarization of incident light showing potential plasmonic effects with only microscale dimensions. These experimental data were analyzed using optical simulation to confirm the response of the devices.

OCIS codes: (230.5160) Photodetectors; (260.5430) Polarization; (250.5403) Plasmonics.
http://dx.doi.org/10.1364/PRJ.3.000001

1. INTRODUCTION

Recently, various photodetection schemes and designs have been proposed [1–5]. The metal-semiconductor-metal (MSM) configuration is among the simplest structures that were implemented in many applications such as high-speed on-chip optical interconnects [6], and optical communication systems [7]. The planar MSM structure consists of metallic electrodes deposited on a semiconductor. With this structure incident photons are detected by the excitation of carriers that drift under the influence of an electric field applied between the electrodes. Metallic electrodes with different shapes and sizes were embedded in the design of photodetectors to enhance their performance [8–10]. The implementation of interdigital metallic electrodes in MSM photodetectors led to an efficient light absorption while also downsizing the device active area [11]. Furthermore, the electrical properties of the photodetector can be improved by increasing the photocurrent, which is achieved by enhancing the rates of photogenerated carriers [12], and reducing the dark current, which is due to the Schottky barriers formed between the metal and the semiconductor [13,14]. Plasmonic enhancement seen in metallic structures may lead to promising applications including surface-enhanced Raman spectroscopy [15], photovoltaics [16,17], and photodetection [18,19]. Typically plasmonic devices consist of nanoscale optical antennas that use surface plasmons to collect and focus light in ultra-small volumes. Properly designing interdigital electrodes not only enhances the electronic characteristics of the photodetectors, but also improves the light absorption of the photodetectors through plasmonic effects [20–23].

The photodetectors investigated in this work operate in the near-infrared region and consist of microscale interdigital metallic electrodes on semi-insulating GaAs. The interdigital electrodes were designed to enhance the electrical and optical properties of the photodetector. Both experimental and simulation studies were performed to fully understand the effect of interdigital electrodes on the device performance. The photocurrent of the devices was found to be several orders of magnitude higher than the dark current. Significant enhancement in the spectral response was observed as the spacing between the interdigital electrodes and the electrode finger-widths are reduced. The spectral response of the devices showed dependence on the polarization of the incident light, which showed maximum spectral response when the incident light was polarized perpendicular to the lengths of the electrode fingers. The experimental results were compared to the results obtained from an optical model.

2. EXPERIMENTAL

The GaAs photodetector device consists of two interdigital finger-like gold electrodes separated by a spacing channel, similar to the structure used in previous work [24]. Figure 1 shows the design schematic of one of the devices. The top view of the device pattern as well as the polarization angle and the polarization directions of the incident light are illustrated in Fig. 1(a). The cross section of the device is represented in Fig. 1(b) and shows metallic electrodes with a width of w spaced by distance d. The ratio between the width of the electrodes and the spacing was designed to be $w = 2d$ for all the devices in this work. Devices with different electrode spacings ($d = 5$, 10, 20, and 50 μm) were fabricated to investigate the effect of reducing the electrodes spacing on the device performance. The interdigital pattern was prepared on a semi-insulating GaAs substrate by standard optical photolithography procedures inside a Class 100 clean room. A photomask was designed for this purpose to generate

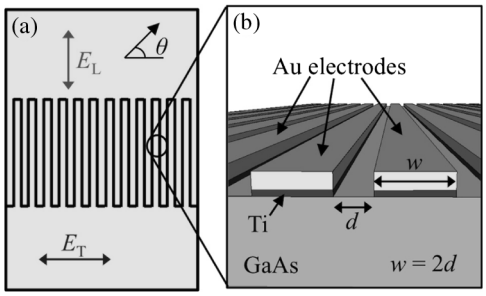

Fig. 1. (a) Schematic of device showing two electrodes (gold) with channels between the interdigital fingers (black). Diagram also shows transverse, E_T, and longitudinal, E_L, polarizations, as well as the polarization angle, θ; (b) cross section of device showing Au electrodes with thickness, w, and spacing, d, attached to the semi-insulating GaAs substrate with the Ti layer.

interdigital patterns with the desired shapes and dimensions. The undoped semi-insulating GaAs substrate has a resistivity of $2.2 \times 10^8\ \Omega \cdot \text{cm}$, and carrier concentration of $5 \times 10^6\ \text{cm}^{-3}$. Then metals (Ti and Au) were deposited on the patterned substrate using electron-beam (e-beam) evaporation. An adhesive layer of Ti with a thickness of 30 nm was first deposited, followed by a Au layer with 50 nm thickness. Wire bonds were created to the interdigital electrodes to enable measuring the photocurrent under different biasing conditions.

The current–voltage ($I - V$) characteristics of the devices were extracted using a Keithley 4200 semiconductor parameter analyzer. The photocurrent was measured under the excitation of a broadband light source that covers the spectral range between 360 and 1800 nm with a power density of 100 mW/cm^2. The spectral response of the devices was measured using a Bruker IFS 125HR Fourier-transform (FT) spectrometer with a quartz beam-splitter. The polarization-dependent measurements were performed using the FT spectrometer and a linear polarizer. The polarizer was used to polarize normal incident light either along the electrodes (longitudinal, E_L) or perpendicular to the electrodes (transverse, E_T). The polarizer was placed on a rotation mount that enables controlling the polarization angle, θ, with reference origin shown in Fig. 1(a).

3. RESULTS

The I–V curve of the GaAs photodetector with an electrode spacing of 5 μm is plotted in Fig. 2(a). At room temperature the dark current of the device was on the order of 10^{-8} A. The dark current was limited to this low order by the high resistivity of the undoped GaAs substrate. Under illumination the photocurrent significantly increases to become several orders of magnitude larger than the dark current. At a bias voltage of 5 V (10,000 V/cm) the dark current was found to be 2.7×10^{-8} A and the photocurrent was 3.7×10^{-3} A. The ratio of the photocurrent to the dark current continues to increase as the biasing voltage increases, and it was 10^5 at a 5 V bias voltage. The same device (with $d = 5$ am) was characterized by calculating its detectivity (D^*) and plotting it as function of the applied bias voltage in Fig. 2(b). Detectivity is one of the important figures-of-merit that enable comparing detectors with different geometries. It was estimated according to the following relation [25]

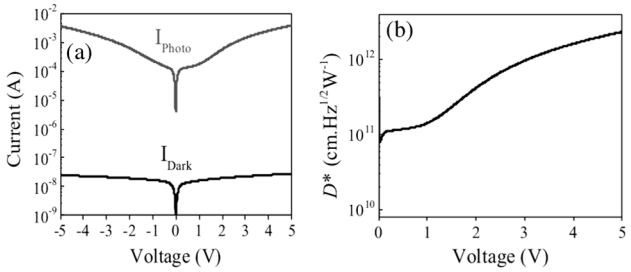

Fig. 2. (a) I–V characteristics of device with 5 μm electrode spacing under illumination intensity of 100 mW/cm^2; (b) detectivity of the device with 5 μm electrode spacing.

$$D* = \frac{I_P \sqrt{A}}{P_{\text{opt}} \sqrt{2qI_D}}, \tag{1}$$

where I_P is the photocurrent, A is the device effective area, P_{opt} is the incident optical power, q is the electron charge, and I_D is the dark current. The device showed high room-temperature detectivity on the order of $2.4 \times 10^{12}\ \text{cmHz}^{1/2}\ \text{W}^{-1}$ at 5 V bias voltage compared with other photodetectors operating in the same spectral region [26,27].

The dependence of the photocurrent on the electrode spacing was investigated by measuring the spectral response of the four different devices with varying electrode spacing, d. Figure 3(a) shows the spectral response, S_R, in arbitrary units for each $d = 5$, 10, 20, and 50 μm with incident light having transverse polarization, E_T. The spectral response has an onset near 900 nm and exhibits rapid decay below 875 nm. The decay in the high-energy spectral region is due to the response of the quartz beam-splitter in the FT spectrometer. These results show that the spectral response increases as the electrode spacing decreases. To further illustrate the relationship between S_R and d, the normalized spectral response at 875 nm (the peak of the response) was plotted as a function of electrode spacing in Fig. 3(b), and the results show that the S_R increases nearly exponentially as the electrode spacing decreases.

To understand why the spectral response changes as a function of the electrode spacing, optical simulations were calculated using the finite-element method (FEM, COMSOL

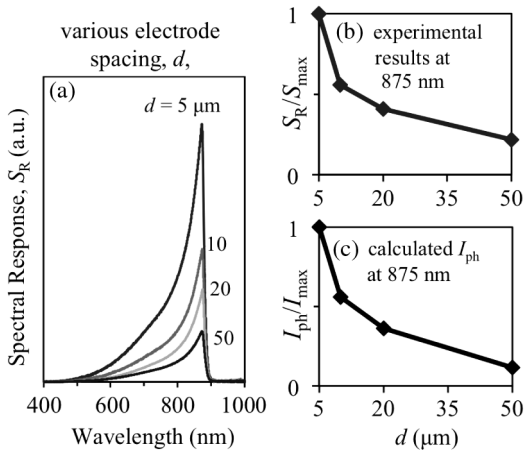

Fig. 3. (a) Spectral response spectra for transverse polarization as function of electrode spacing, d; (b) normalized peak from (a) plotted as function of electrode spacing; (c) normalized calculated photocurrent as a function of electrode spacing at 875 nm incident light.

4.4) similar to previous work [28]. First the optical response of the interdigital electrode array was modeled with normal incident transversely polarized light similar to the experimental results in Figs. 3(a) and 3(b). The model calculated the local electric field, E_{loc}, of the device due to the incident light with wavelength of 875 nm. Then the sum of the local electric field squared, over the entire GaAs cross sectional area for one period was calculated and defined as Φ

$$\Phi = \sum E_{\text{loc}}^2, \tag{2}$$

to simplify subsequent equations. The cross sectional area of GaAs is $A_\Lambda = a\Lambda$, where a is the height of GaAs in the model, which was selected to be a value that is much greater than the skin depth of GaAs ($a = 27$ μm for this model), and the period length is $\Lambda = w + d = 3d$. The photocarrier generation rate (G_0) in the GaAs is then calculated by

$$G_0 = \frac{cn\varepsilon_0}{2\,h\nu A_\Lambda}\Phi, \tag{3}$$

where c is the speed of light, n is the refractive index of GaAs, ε_0 is the vacuum permittivity, h is Planck's constant, and ν is the frequency of light with wavelength of 875 nm. From here the photoconductive current (I_P) can be calculated by

$$I_P = \mathrm{q}wlG_0\tau(\mu_n + \mu_p)\frac{V}{d}, \tag{4}$$

where l is the total length of all the electrode fingers that are illuminated by the incident light, τ is the decay time of GaAs, μ_n and μ_p are the mobility of the carriers, and V is the applied bias voltage. Photocurrents for each electrode spacing at 875 nm were calculated with this computational model, then normalized by the maximum calculated current value and plotted in Fig. 3(c). These results match very well with the experimental results in Fig. 3(b).

Several factors affect the photocurrent as the electrode spacing, d, is reduced. First, the sum of the length of all the electrodes which are illuminated, l, increases as d decreases. Since a smaller d increases the density of the electrodes under illumination, then the number of periods that are illuminated increases, and therefore l increases. Second, Φ in Eq. (2) decreases as d is reduced since the GaAs cross sectional area decreases. However, this is not a perfectly linear relationship since there are small plasmonic enhancements at the edge of the electrodes. This generates a slightly larger overall E^2 density in the GaAs for the smaller electrodes. Finally, another factor is the static electric field that exists between the two electrodes, $E = V/d$, due to the constant applied bias voltage. As the electrode spacing decreases, this applied electric field increases. All these factors contribute to the overall increase in the photocurrent as the electrode spacing decreases.

Second, polarization-dependent measurements were performed to study the role of potential plasmonic activity in enhancing the response. The spectral response measurements were performed while the polarization of incident light was switched between transverse and longitudinal directions. Figure 4(a) depicts the dependence of spectral response on the polarization of incident light for a device with an electrode spacing of 5 μm. When the incident light was polarized normal to the electrodes, E_T, a larger response was obtained. However, when the electric field was rotated 90° and aligned parallel to the electrodes, E_L, the response was reduced significantly. This indicates strong dependence of the spectral response on the polarization of the incident light.

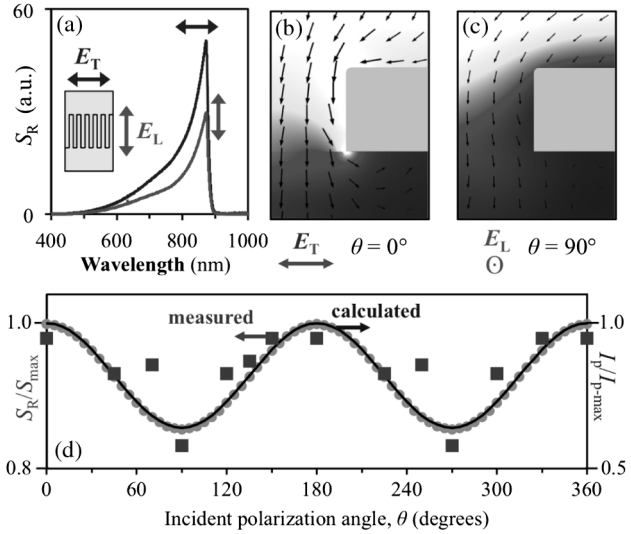

Fig. 4. (a) Measured spectral response of a 5 μm device for transverse and longitudinal polarization; (b) calculated optical enhancement near the electrode edge for transverse polarization; (c) calculated optical enhancement near the electrode edge for longitudinal polarization; (d) polarization-dependent normalized spectral response measurements (squares) and normalized photocurrent calculations (circles) with a $A\cos^2\theta + B$ fit (line).

The polarization dependence of the spectral response exhibited by experimental results was investigated by modeling a 5 μm electrode spaced device and varying the polarization angle of the incident light, θ, between transverse ($\theta = 0°$) and longitudinal ($\theta = 90°$) every 5°. The calculated optical enhancement near the edge of the electrode is shown in Figs. 4(b) and 4(c) for transverse (E_T) and longitudinal (E_L) polarization, respectively. Figure 4(b) shows that more light is scattered into the GaAs near the edge of the electrode for transverse incident light compared to longitudinal incident light in Fig. 4(c). This is likely due to surface plasmonic effects at the edge of the gold electrode and this polarization dependence has similar behavior to other nanoscale plasmonic devices [15,20–23].

The normalized photocurrent due to the incident light was calculated for each incident polarization angle and the results are plotted in Fig. 4(d) along with the normalized measured polarization dependent spectral response at 875 nm. For devices with a 5 μm electrode spacing, the polarization ratio, $r_S = S_T/S_L$, of the transverse spectral response (S_T) to the longitudinal response (S_L) is 1.7 for the device in Fig. 4(a) and 1.2 for the device in Fig. 4(d). The polarization ratio, $r_I = I_T/I_L$, of the simulated transverse photocurrent (I_T) to the longitudinal photocurrent (I_L) for a $d = 5$ μm device was calculated to be $r_I = 1.5$. This result matches with the experimental polarization ratio, r_S.

4. CONCLUSIONS

In conclusion, this work demonstrates that devices with relatively large electrode widths show polarization dependence that is comparable to nanostructure devices [15,20–23]. Even

though the plasmonic effects of microscale structures are small compared to the enhancement in nanoscale devices, they can enhance the response. Especially when having a large array of gold microstructures that are used as electrodes, these effects are multiplied and become more pronounced. The devices exhibited enhancement in the electronic properties, in which the dark current was limited to the order of 10^{-8} A, while the photocurrent was measured to be 5 orders of magnitude higher than the dark current at a bias voltage of 5 V. The room temperature detectivity extracted from the photocurrent and dark current is estimated to be on the order of 2.4×10^{12} cmHz$^{1/2}$ W^{-1} at 5 V bias voltage. Microscale interdigital electrodes on MSM photodetectors improved both the electrical and optical properties of these devices. By carefully studying and characterizing how the geometry of the electrodes affects these characteristics, this work has determined important design considerations for future interdigital electrode devices.

ACKNOWLEDGMENTS

This work was supported by the Air Force Office of Scientific Research (Grant No. FA9550-10-1-0136) and NASA (Grant No. 242026-1BBX11AQ36A). The work of one of the authors (A. M. Hill) was supported by a University of Arkansas Honors College Undergraduate Research grant. The authors would like to thank the Microelectronics–Photonics program at the University of Arkansas for the COMSOL license.

REFERENCES

1. Y. Yuan, Q. Dong, B. Yang, F. Guo, Q. Zhang, M. Han, and J. Huang, "Solution-processed nanoparticle super-float-gated organic field-effect transistor as un-cooled ultraviolet and infrared photon counter," Sci. Rep. **3**, 02707 (2013).
2. O. Lopez-Sanchez, D. Lembke, M. Kayci, A. Radenovic, and A. Kis, "Ultrasensitive photodetectors based on monolayer MoS_2," Nat. Nanotechnol. **8**, 497–501 (2013).
3. G. Konstantatos and E. H. Sargent, "Nanostructured materials for photon detection," Nat. Nanotechnol. **5**, 391–400 (2010).
4. J. R. Retamal, C.-Y. Chen, D.-H. Lien, M. Huang, C.-A. Lin, C.-P. Liu, and J.-H. He, "Concurrent improvement in photogain and speed of a metal oxide nanowire photodetector through enhancing surface band bending via incorporating a nanoscale heterojunction," ACS Photon. **1**, 354–359 (2014).
5. P. Hu, Z. Wen, L. Wang, P. Tan, and K. Xiao, "Synthesis of few-layer GaSe nanosheets for high performance photodetectors," ACS Nano **6**, 5988–5994 (2012).
6. S. Assefa, F. Xia, and Y. A. Vlasov, "Reinventing germanium avalanche photodetector for nanophotonic on-chip optical interconnects," Nature **464**, 80–84 (2010).
7. M. Y. Liu and S. Y. Chou, "Internal emission metal-semiconductor-metal photodetectors on Si and GaAs for 1.3 μm detection," Appl. Phys. Lett. **66**, 2673–2675 (1995).
8. H.-H. Chen, Y.-C. Su, W.-L. Huang, C.-Y. Kuo, W.-C. Tian, M.-J. Chen, and S.-C. Lee, "A plasmonic infrared photodetector with narrow bandwidth absorption," Appl. Phys. Lett. **105**, 023109 (2014).
9. P. Fan, U. K. Chettiar, L. Cao, F. Afshinmanesh, N. Engheta, and M. L. Brongersma, "An invisible metal–semiconductor photodetector," Nat. Photonics **6**, 380–385 (2012).
10. L. Cao, J.-S. Park, P. Fan, B. Clemens, and M. L. Brongersma, "Resonant germanium nanoantenna photodetectors," Nano Lett. **10**, 1229–1233 (2010).
11. S. Collin, F. Pardo, R. Teissier, and J.-L. Pelouard, "Efficient light absorption in metal–semiconductor–metal nanostructures," Appl. Phys. Lett. **85**, 194–196 (2004).
12. G. Konstantatos and E. H. Sargent, "Solution-processed quantum dot photodetectors," Proc. IEEE **97**, 1666–1683 (2009).
13. G. Konstantatos, I. Howard, A. Fischer, S. Hoogland, J. Clifford, E. Klem, L. Levina, and E. H. Sargent, "Ultrasensitive solution-cast quantum dot photodetectors," Nature **442**, 180–183 (2006).
14. R.-P. Chang and D.-C. Perng, "Near-infrared photodetector with $CuIn_{1-x}Al_xSe_2$ thin film," Appl. Phys. Lett. **99**, 081103 (2011).
15. J. B. Herzog, M. W. Knight, Y. Li, K. M. Evans, N. J. Halas, and D. Natelson, "Dark plasmons in hot spot generation and polarization in interelectrode nanoscale junctions," Nano Lett. **13**, 1359–1364 (2013).
16. J. N. Munday and H. A. Atwater, "Large integrated absorption enhancement in plasmonic solar cells by combining metallic gratings and antireflection coatings," Nano Lett. **11**, 2195–2201 (2011).
17. H. A. Atwater and A. Polman, "Plasmonics for improved photovoltaic devices," Nat. Mater. **9**, 205–213 (2010).
18. M. W. Knight, H. Sobhani, P. Nordlander, and N. J. Halas, "Photodetection with active optical antennas," Science **332**, 702–704 (2011).
19. P. Fan, K. C. Y. Huang, L. Cao, and M. L. Brongersma, "Redesigning photodetector electrodes as an optical antenna," Nano Lett. **13**, 392–396 (2013).
20. H. Chalabi, D. Schoen, and M. L. Brongersma, "Hot-electron photodetection with a plasmonic nanostripe antenna," Nano Lett. **14**, 1374–1380 (2014).
21. F.-F. Ren, K.-W. Ang, J. Song, Q. Fang, M. Yu, G.-Q. Lo, and D.-L. Kwong, "Surface plasmon enhanced responsivity in a waveguided germanium metal-semiconductor-metal photodetector," Appl. Phys. Lett. **97**, 091102 (2010).
22. J. Hetterich, G. Bastian, N. A. Gippius, S. G. Tikhodeev, G. von Plessen, and U. Lemmer, "Optimized design of plasmonic MSM photodetector," IEEE J. Quantum Electron. **43**, 855–859 (2007).
23. B. Y. Zheng, Y. Wang, P. Nordlander, and N. J. Halas, "Color-selective and CMOS-compatible photodetection based on aluminum plasmonics," Adv. Mater. **26**, 6318–6323 (2014).
24. A. I. Nusir, J. Aguilar, Z. Bever, and M. O. Manasreh, "Uncooled photodetectors based on CdSe nanocrystals with an interdigital metallization," Appl. Phys. Lett. **104**, 051124 (2014).
25. K.-J. Baeg, M. Binda, D. Natali, M. Caironi, and Y.-Y. Noh, "Organic light detectors: photodiodes and phototransistors," Adv. Mater. **25**, 4267–4295 (2013).
26. K. Swaminathan, T. J. Grassman, L.-M. Yang, Q. Gu, M. J. Mills, and S. A. Ringel, "Optically-aligned visible/near-infrared dual-band photodetector materials and devices on GaAs using metamorphic epitaxy," J. Appl. Phys. **110**, 063109 (2011).
27. L. Fu, P. Lever, K. Sears, H. H. Tan, and C. Jagadish, "In0.5-Ga0.5As/GaAs quantum dot infrared photodetectors grown by metal-organic chemical vapor deposition," IEEE Electron. Device Lett. **26**, 628–630 (2005).
28. A. M. Hill, A. I. Nusir, P. V. Nguyen, O. M. Manasreh, and J. B. Herzog, "Computational electromagnetic analysis of plasmonic effects in interdigital photodetectors," Proc. SPIE **9163**, 91633Q (2014).